Preserving tracer correlations in atmospheric transport models

Robert McGraw[1], Fan Yang[1] and Laura M. Fierce[2]

[1]Environmental and Climate Sciences Department, Brookhaven National Laboratory, Upton NY 119073
[2]Atmospheric Sciences and Global Change, Pacific Northwest National Laboratory, Richland, WA 99354

Abstract

A linear non-diffusive algorithm for advective transport is developed that greatly improves the level of detail at which aerosols and clouds can be represented in atmospheric models. Linear advection schemes preserve tracer correlations but the basic linear scheme, employing zeroth-order finite differencing, is rarely used by atmospheric modelers on account of its excessive numerical diffusion. Higher-order schemes are in widespread use, but these present new problems as nonlinear adjustments are required to avoid occurrences of negative concentrations, spurious oscillations, and other non-physical effects. Generally successful at reducing numerical diffusion during the advection of individual tracers, e.g. particle number or mass, the higher-order schemes fail to preserve even the simplest correlations between interrelated tracers. As a result, important tracer attributes of aerosol and cloud populations including radial moments of particle size distributions, molecular precursors related through chemical equilibria, aerosol mixing state, and distribution of cloud phase are all poorly represented in models. We introduce a new scheme, minVAR, that is both non-diffusive and preservative of tracer correlations, thereby combining the best features of the basic and higher-order schemes while enabling new features such as the tracking of sub-grid information at arbitrarily fine scales with high computational efficiency.

Plain Language Summary: In this paper we resolve a long-standing bottleneck to the representation of aerosols and clouds in atmospheric models beyond the two-moment microphysical schemes currently in use. The bottleneck is caused by the failure of higher-order advection schemes to preserve correlations between interrelated tracers during transport – a task for which they were never designed. The paper was motivated in part by our recent convective cloud chamber study [Yang et al., 2022], which employed a second-

order advection scheme and a two-moment cloud microphysical scheme limited to tracking particle number and mass. The new approach introduces a diffusion limiter, under the idea that achieving minimal spatial variance on an Eulerian model grid implies maximal resolution and elimination of numerical diffusion. By preserving tracer correlations and eliminating numerical diffusion, *minVAR* – short for minimum variance – includes the best features of the basic linear and higher-order schemes. This innovation resolves the two-moment bottleneck, a necessary step for high-fidelity, multi-moment representation of aerosols and clouds in atmospheric models.

1. Introduction

The present study was motivated by the need to preserve correlations between interrelated tracers throughout the advection process as it is represented in Eulerian models. Such correlations affect the sequences of radial moments used to track particle size distributions, apportionment of reactive chemical species affecting aerosol composition and mixing state, and tracking of cloud phase. Fully-linear advection schemes rigorously preserve these correlations, but on account of extensive numerical diffusion find their application limited to the modeling of laboratory- and industrial-scale reactors, cloud chambers, and other systems where high-resolution grids and fine time stepping can affordably be used.

The basic linear scheme, which employs zeroth-order finite differencing, has advantages, not the least of which are linear superposition, preservation of correlation, freedom from dispersion, and high computational efficiency, but is generally deemed too diffusive by the atmospheric community for use, especially with the coarse grids of models operating at regional to global scales. Instead, higher-order finite-differencing schemes are in widespread used. Examples include the Bott scheme, based on polynomial interpolation of concentrations in neighboring grid cells [Bott, 1989a, b], the slopes method, which preserves the zeroth and first-order spatial moments [Russell and Lerner, 1981], and its successor the quadratic upstream (QUS) advection scheme, which conserves zeroth, first, and second-order spatial moments [Prather, 1986]. These higher-order schemes do an

excellent job reducing numerical diffusion during the advection of independent tracers, but were never designed to preserve correlations between the tracers from an interrelated set. Moreover, the higher-order schemes tend to be complex, tedious to follow, and prone to numerical artifacts. The latter can include failure to preserve positivity, monotonicity, and stability. Nonlinear fixes can serve to eliminate these artifacts, but such modifications only worsen the tracer correlation problem, increase code complexity, and reduce computational speed.

Sources of the failure to preserve physically-based correlations between the lower-order radial moments of a particle population were analyzed by Wright [2007] and attributed largely to the fact that the higher-order advection schemes track spatial gradients that differ for different moments, resulting in dispersion, unphysical size distributions, and corruption of moment sets. Wright examined moment failures for the Bott [1989a, b] and QUS [Prather, 1986] advection schemes using ensembles of 10^4 test cases spanning a range of initial conditions and flow velocities. The Prather scheme performed somewhat better in this regard, but both gave rise to unphysical moment sets at frequencies $\geq 0.7\%$. The problem is not limited to moments. For example, when three species initially with constant sum were advected separately in a one-dimensional constant velocity flow, local errors in the sum ranged from order 10% and up to 30% when cloud-like interactions were considered [Ovtchinnikov and Easter, 2009]. The aforementioned limitations have huge impact on the representation of aerosol and cloud properties and processes in atmospheric models. They are largely responsible for two-moment aerosol and cloud microphysical schemes, and modal methods, currently limited to tracking aerosol number and mass while having to prescribe variance, remaining state of the art. As a result, process-level understanding gained through laboratory measurements and field observations remains largely underutilized due to the limited capacity of the models to include it.

There have been a few attempts, none entirely successful, aimed at correcting corrupted moment sequences [Wright, 2007; McGraw, 2007, 2012; Ovtchinnikov and Easter, 2009]. The present study shifts focus from correcting miscalculated moment sequences produced by the higher-order schemes to limiting numerical diffusion in the basic scheme.

This paper was motivated in part by our recent convective cloud chamber study [Yang et al., 2022], which employed a second-order advection scheme and a two-moment cloud microphysical scheme limited to tracking particle number and mass. The new approach introduces a diffusion limiter to the basic scheme, with the idea that achieving minimal spatial variance on Eulerian grids achieves maximal resolution and elimination of numerical diffusion. By preserving tracer correlations and eliminating numerical diffusion, minVAR, short for minimum variance, blends the best features of the basic and higher-order schemes thereby breaking the two-moment bottleneck necessary for high-fidelity (multi-moment) representation of aerosols and clouds in atmospheric models.

Section 2 gives a brief preview of the proposed scheme, minVAR and its comparison to two others, the basic and QUS schemes. Section 3 focuses on methods, introducing optimization theory in the form of an intuitive linear program (LP) to develop minVAR's minimal spatial variance solutions on an Eulerian grid. This is followed by presentation of a closed-form analytic solution that is computationally faster and fully LP-equivalent. Section 4 focuses on applications. Calculations illustrate the encoding of arbitrarily fine scale features from a spatially-dispersed particle cloud onto the coarse grid, while tracking such features at scale with particle-by-particle resolution. A sparse, four-point adaptive quadrature representation of the same cloud is also presented. Most importantly, it is shown that contributions to spatial variance from *physical* processes add linearly to minVAR and are (to within numerical precision) separable from it. In other words the two variances, one inherent to the mathematical representation of points on a grid (Sec. 3), the other physical (Sec. 4), can be separately identified and individually tracked. Finally, minVAR is applied to the advection of interrelated tracer sets from an external mixture of three distinct aerosol types following a test case introduced by Wright [2007]. Recovery of each aerosol type at any stage of the calculation is obtained by least-squares projection onto the vector space spanned by the identifying moment sequence vectors, one for each aerosol type, with zero residual. Section 5 presents a summary and discussion of the new approach.

2. Preview of minVAR and comparison with the basic and QUS advection schemes

This section presents a graphical preview of minVAR showing similarities and contrasts between it and the basic and QUS schemes. The details of how minVAR works are covered in Sec. 3.

Advection of a pulse. Consider the advection of a pulse, consisting initially of a unit amount of tracer material in a single grid cell in a constant velocity one-dimensional flow. The Courant number is set at:

$$c = \frac{u\Delta t}{\Delta X} = 0.15, \tag{1}$$

where u is wind speed in the positive x direction, Δt is timestep, and ΔX is the uniform width of each grid cell along the x coordinate. For rational Courant numbers and linear non-

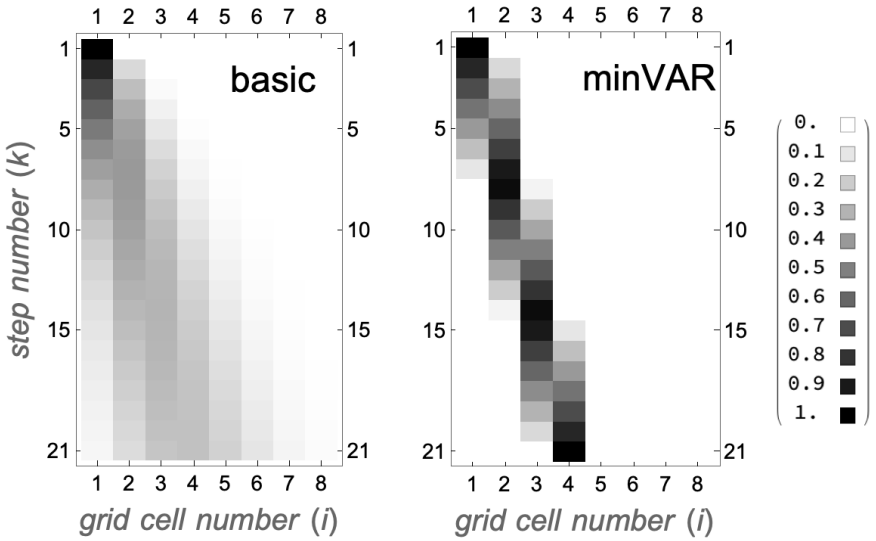

Fig. 1. Comparing results from the advection of a single pulse according to the two linear advection schemes. Initial condition: Grid cell 1 filled, others empty. The figure shows results through 20 advection steps with wind direction to the right and $c = 0.15$. Left panel, basic zeroth-order finite difference scheme. Right panel, minVAR scheme with the new diffusion limiter in place. Distributions are normalized to unity with grayscale values indicated in the legend.

diffusive advection, the perfect-shift property is encountered after an integer number of grid spacings, resulting in exact pulse recovery. For example, for $c = 0.15$, an integer shift of 3 grid spacings is obtained after twenty time steps ($20 \times 0.15 = 3$) as illustrated, in the

mean, for the basic scheme, and with exact pulse recovery for the non-diffusive, non-dispersive minVAR scheme in Fig. 1.

Density profiles in the basic scheme follow a normalized Bernoulli distribution having mean travel distance $\mu_x(n) = n\,c$, with $\mu_x(0) = 1$ in the present example (cf. Fig. 1), and variance, $\mathrm{var_x} = n\,c\,(1 - c)$. n is the number of completed advection such that $n = k - 1$ for step number k as plotted in Fig. 1. With increasing n, the Bernoulli distribution rapidly approximates a normalized Gaussian having these same formulaic values for mean and variance [Chandrasekhar, 1943]. The minVAR solution has the same mean $\mu_x = n\,c$, and an analytic expression for its variance is developed in Sec. 3. The minVAR solution exhibits exact pulse recovery at $n = 20$ ($k = 21$) and an evenly split pulse of maximal minVAR between grid cells 2 and 3 at $n = 10$ ($k = 11$).

The exact position after n completed advection steps, $\mu_x(n)$, is given correctly in both linear schemes by the centroid of the distributions shown in Fig. 1. From exact pulse recovery seen in the figure it is evident that minVAR is completely non-diffusive. Moreover the minVAR distributions are reversable with reversal of wind speed and direction, yielding recovery of the original pulse in grid cell 1. This is not the case with the basic scheme as the variance continues its linear increase with n irrespective of the change in wind direction due to the irreversibility of numerical diffusion in the basic scheme. Nevertheless, the centroids of the distributions track perfectly and are restored to their original value in both schemes.

Figure 2 shows application to a frontal distribution. The frontal distribution, which results from advection of a train of pulses arriving from the left, serves to illustrate the superposition principal for linear advection schemes, here the diffusive basic and non-diffusive minVAR schemes, solid and dashed histograms, respectively.

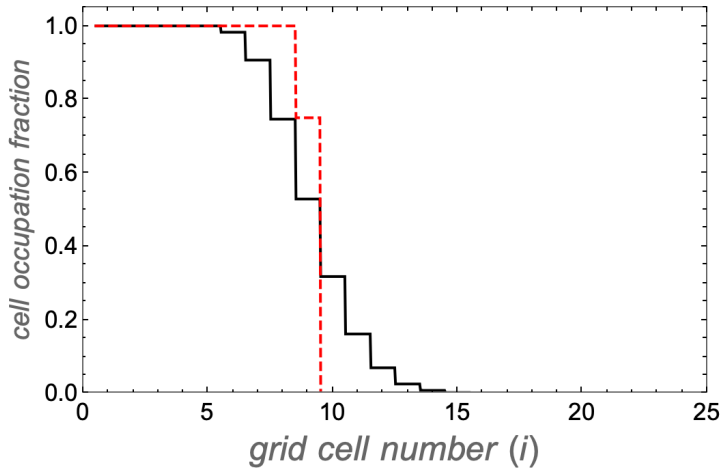

Fig. 2. Comparing results from advection of a tracer front. Initial condition: Grid cells 1-5 filled others empty. Results after 25 advection steps with replacement from the left. Curves: Linear advection with (dashed), and without (solid) the minVAR diffusion limiter in place. Both curves average to give the exact travel distance of the front, equal to 3.75 cell widths for c = 0.15.

Figure 3a shows a direct comparison of the minVAR and QUS advection results after 70 advection steps for the same initial unit pulse as Fig. 1. The minVAR solution, dashed, is an evenly split pulse of maximal minVAR between grid cells 11 and 12 after an average travel distance of 10.5 cell widths. QUS and minVAR each performed well in this single-tracer test, with QUS showing only a small amount of numerical diffusion in the wings of its histogram. Figure 3b is a comparison of the three methods. A rapid and linearly increasing variance with step number is seen for the basic scheme, as expected from the binomial distribution. The

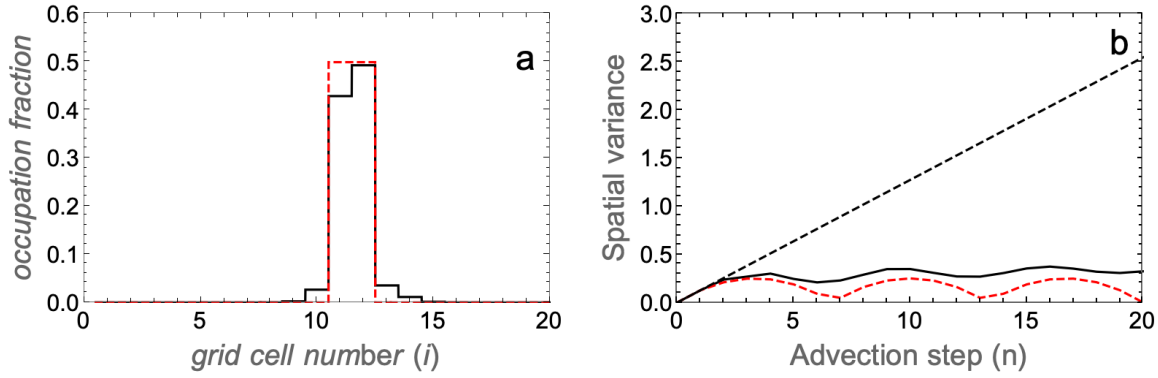

Fig. 3. (a) Comparison of pulse shape after 70 advection steps. Histograms of cell occupation fraction for the QUS (solid) and minVAR (dashed) advection schemes. (b) Comparing evolution of spatial variance for the three models from 0 to 20 advection steps: dashed black line (basic scheme), solid curve (QUS), dashed red curve (minVAR). The Courant number is unchanged from Figs. 1 and 2.

Solid and dashed curves for QUS and minVAR, respectively, tend to flatten out, indicating that numerical diffusion is controlled in both schemes. All three models agree after the first time step, before higher-order QUS gradient terms are evaluated.

As reversibility and exact pulse recovery imply, minVAR is completely non-diffusive. Consequently, the vertical distance between the QUS and minVAR curves of Fig. 3b provides a measure of numerical diffusion in the QUS scheme at each advection step. Similarly for the basic scheme, with its much higher and growing level of numerical diffusion, reflected in the difference between the line and minVAR curve. The minVAR variance itself is attributed to a purely mathematical effect innate to the Eulerian representation of the coordinates of a zero-dimensional point as it moves across the grid. This requires a minimum of two adjacent grid cells per coordinate to precisely locate the point's position within its home cell, except in special cases of perfect reconstruction where fewer cells are required. Whereas innate variance is solely responsible for shaping the minVAR curve, the QUS scheme carries a vestige of this mathematical effect seen in the smaller oscillations with step number visible in the solid curve. A small phase shift with respect to the minVAR oscillation is also evident and is due to dispersion in the QUS scheme. Dispersion, together with the conditionally switched-on nonlinearities associated with flux limitation and filling, are largely responsible for destroying tracer correlations in the higher-order models — not numerical diffusion. The basic scheme, though most diffusive of the three, fully preserves tracer correlations.

3. The minVAR diffusion limiter for advection on Eulerian grids

3.1 Optimization approach based on linear programming (LP). The problem of finding minimal variance representations for locating points on a grid has a simple and unique solution obtainable by linear optimization methods. Tables 1 and 2 give linear programs (LPs) for limiting numerical diffusion through constrained variance minimization on one and two dimensional grids. Time-dependent point coordinates $\{x, y\}$ are indicated in vector form as pulse-mean values $\{\mu_x(t), \mu_y(t)\}$ on the grid. For advection schemes based on finite differencing, calculations are performed on a stencil moved across the grid. minVAR employs finite volumes with calculations carried out on a three by three plaquette of nine grid cells

moved across the grid (Fig. 4). Solutions in one dimension may be obtained by projecting the plaquette onto the *x*- or *y*- coordinate axis, or directly using three-grid-cell central slices parallel to the *x*- or *y*- coordinate axis of the plaquette. The method is quite flexible: A calculation of Fig. 1, linked to in the open research statement, employs eight grid cells along the *x*- axis instead of the three shown in Table 1.

The two-coordinate LP of Table 2 is a natural extension of the one-coordinate program of Table 1. The number of occupied grid cells in the solution plaquette equals the number of equality constraints (except in special cases of perfect reconstruction where it is less). In one dimension these are the normalization and position constraints and the solution

---

Table 1. Linear Program for one-dimensional grids: $LP_{1D}[\mu_x(t)]$
p$[i]$ is the occupation fraction of normalized material in grid cell i centered at x_i.

Minimize variance cost function: $\sum_{i=1}^{3} x_i^2\, p[i] \; - \; \mu_x^2(t)$
subject to:
normalization constraint: $\sum_{i=1}^{3} p[i] = 1$
x-position constraint: $\sum_{i=1}^{3} x_i\, p[i] = \mu_x(t)$

inequality constraints: $0 \leq p[i]$ for each i.

Table 2. Linear Program for two-dimensional grids: $LP_{2D}[\mu_x(t), \mu_y(t)]$
p$[i]$ is the occupation fraction of normalized material in grid cell i centered at $\{x_i\, , y_i\}$.

Minimize variance: $\sum_{i=1}^{9}(x_i^2 + y_i^2)p[i] \; - \; (\mu_x^2(t) + \mu_y^2(t))$
subject to:
normalization constraint: $\sum_{i=1}^{9} p[i] = 1$
x-position constraint: $\sum_{i=1}^{9} x_i\, p[i] = \mu_x(t)$
y- position constraint: $\sum_{i=1}^{9} y_i\, p[i] = \mu_y(t)$
zero covariance constraint: $\sum_{i=1}^{9} x_i\, y_i\, p[i] = \mu_x(t)\mu_y(t)$

inequality constraints: $0 \leq p[i]$ for each i.

---

is unique. In two dimensions the zero covariance condition has been added as a fourth equality constraint. This choice yields four occupied grid cells making the solution unique while, at the same time, recovering the results from orthogonal back projections of the 1D x and y solutions (Fig. 4). Quadratic terms $\mu_x^2(t)$, appearing in the cost function, and $\mu_x(t)\mu_y(t)$ in the covariance constraint, are constant point-position arguments for each call to the program and do not affect linearity of the method.

Figure 4a shows our convention for the plaquette-square occupation fractions appearing in the program. The nine square centers used in the 2D program take on integer coordinate values $\{x_i\} = \{0,1,2,0,1,2,0,1,2\}$, $\{y_i\} = \{0,0,0,1,1,1,2,2,2\}$, covariance coefficients $\{x_i y_i\} = \{0,0,0,0,1,2,0,2,4\}$, and second moment coefficients $\{x_i^2 + y_i^2\} = \{0,1,4,1,2,5,4,5,8\}$. Solutions are reported using the convention:

$$LP_{2D}\left[\mu_x(t), \mu_y(t)\right] = \left\{minVAR, \{p[1], p[2], p[3], p[4], p[5], p[6], p[7], [8], p[9]\}\right\} \qquad (2a)$$

where minVAR is the sought for minimum variance and p[1] thru p[9] are the minVAR grid occupation numbers normalized to unity.

Figure 4b illustrates a specific solution. The lower right corner cells of the plaquette, (cells 2,3,5 and 6) contain minVAR's Eulerian representation of the selected point, coordinates of which are indicated by the red marker, along a hypothetical wind trajectory (red curve). Grid occupation numbers are illustrated using the grayscale of Fig. 1 with numerical values given in Eq. 2b. Cell 3, with $p[3] = 0.014$, appears empty in grayscale as its value is below the shading threshold. The trajectory is representative of one that might be input to the advection routine from a separate computational fluid dynamics code or meteorological model. Using coordinates of the selected point as an example, $x = \mu_x(t) = 1.07292$, $y = \mu_y(t) = 0.808117$, the solution from Table 2 is:

$$LP_{2D}[x, y] = LP_{2D}[1.07292, 0.808117] =$$

$$\{0.222667, \{0, 0.177891, 0.0139921,\ \ 0, 0.749189, 0.0589279, 0, 0, 0\}\}. \qquad (2b)$$

The $p[i]$'s listed in 2b, satisfy the four equality and nine inequality constraints of Table 2, as do many other solutions. What makes this solution unique is that it also minimizes the cost function to give the minimum possible variance representation of the test point's location on the grid. The centroid, or center of mass of the spread, matches the arguments of the LP, its minVar variance (0.222663) is consistent with the $p[i]$ values listed in 2b. While a single point by itself has no intrinsic variance, its Eulerian representation does. Section 4 generalizes this idea from single points to clouds of points having physical variance added to but separable from minVAR.

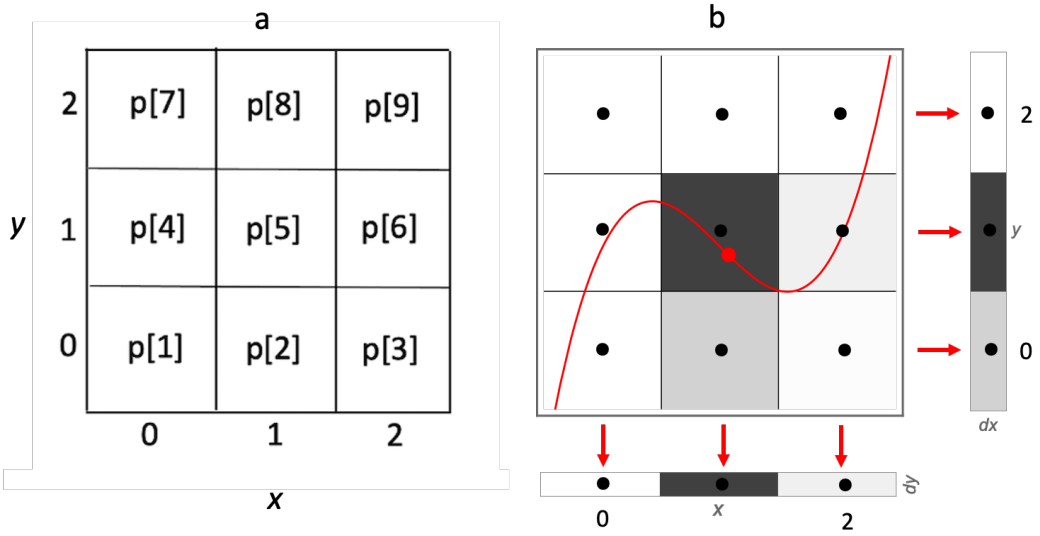

Fig. 4. (a) The basic three by three plaquette showing orientation of *x*- and *y*- axis and numbering of grid squares. (b) grayscale representation of densities/occupation number fractions within the plaquette. The red curve depicts a wind trajectory, and a point along that trajectory having coordinates given in Eq. 2b corresponding to the centroid of the densities shown. Row and column projections (red arrows) and back projections are discussed in the text.

Finally it should be noted that central slices from the 2D result recover the 1D forward projections depicted by the arrows in Fig, 4b. Specifically, in notation of Eq. 2, $\mathrm{LP}_{1\mathrm{D}}(x) = \mathrm{LP}_{2\mathrm{D}}(x, 1)$ and $\mathrm{LP}_{1\mathrm{D}}(y) = \mathrm{LP}_{2\mathrm{D}}(1, y)$. More generally $\mathrm{LP}_{2\mathrm{D}}(x, y) = \mathrm{LP}_{1\mathrm{D}}(x) + \mathrm{LP}_{1\mathrm{D}}(y)$. Results of this type are trivial to prove using a closed-form analytic solution that will now be derived. In contrast to the LP instruction set, the analytic solution, though simpler and much faster to compute, is less intuitive and far less general. Derivation of the analytic result was

motivated by the LP-generated contour plots of Fig. 5, suggesting the use of LP as a development tool. Both solutions, while numerically equivalent are computationally very different. For these reasons it is of value to retain both derivations for perspective on the new approach.

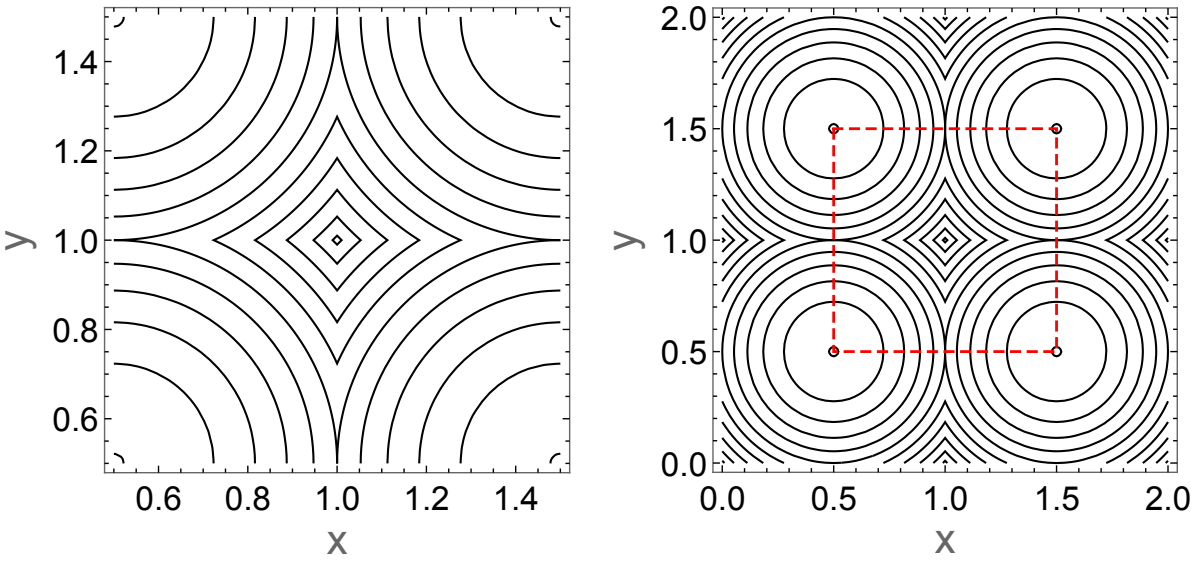

Fig. 5. Contours of constant minVAR in 2D. Left, center square of a 9-square plaquette showing contours as a function of point position $\{x, y\} = \{\mu_x, \mu_y\}$. Contour values from center to corners are 0.01, 0.05, 0.10, 0.15, 0.20, 0.25, 0.30, 0.35, 0.40, 0.45, 0.499. The first and last entries mark the near center and near corner positions, respectively. Horizontal and vertical lines through the center having coordinates {x, 1} and {1, y} (not shown) recover variances along the 1D x and y coordinates, as special cases of the 2D solution. Right, stacking of four adjacent cells showing periodicity and continuity across grid cell boundaries. Red square, corners and boundaries of the center square shown on the left.

3.2 LP-equivalent analytic solution and extension to three coordinate dimensions: The left panel of Fig. 5 shows contours of constant minVAR (see caption) for the center square of the plaquette as computed from LP_{2D}. The right panel shows the center square, highlighted in red, imbedded in a larger area of four cells illustrating translational symmetry and toroidal boundary conditions of the underlying grid.

Guided by the radial symmetries exhibited in the minVAR contours of Fig. 5, a closed-form analytic solution for computing minVAR was developed and is presented in Table 3. One sees immediately the importance of the corners of each cell, $\{a_x, a_y\}$, serving as centers

for the circles of constant minVAR. The lead coefficient on the right for the 1D case, $1/4$, is the squared distance from the nearest edge of the grid cell to its center for one coordinate. For two and three coordinates it's the squared distance from the nearest corner of the grid cell to its center. In three dimensions the squared distance corner to center is $(\sqrt{3}/2)^2 = 3/4$. The subtracted term is the squared Euclidean distance from the nearest edge (or corner) to the point being represented.

Table 3. Closed-form analytic formulae for minVAR values and back projected densities.

<u>minVAR values in one, two, and three dimensions</u>

1D: $mV_{1D}(x) = 1/4 - \Delta_x^2$ where $\Delta_x^2 = (a_x - x)^2$
2D: $mV_{2D}(x,y) = 1/2 - (\Delta_x^2 + \Delta_y^2)$ $\Delta_y^2 = (a_y - y)^2$
3D: $mV_{3D}(x,y,z) = 3/4 - (\Delta_x^2 + \Delta_y^2 + \Delta_z^2)$ $\Delta_z^2 = (a_z - z)^2$

$\{a_x, a_y, a_z\} = \{Floor[x] + 1/2, Floor[y] + 1/2, Floor[z] + 1/2\}$
$Floor[x]$ gives the greatest integer less than or equal to x

<u>Back-projection formula for plaquette densities in 2D</u>

$\text{mat} = \{\{1,1,1\},\{0,1,2\},\{0,1,4\}\}$ (3×3 moment matrix for the reference plaquette of 4a)
$\text{mat}^{-1} = \{\{1,-3/2,1/2\},\{0,2,-1\},\{0,-1/2,1/2\}\}$(mat inverse)

$v1D(x) = \{1, x, mV_{1D}(x) + x\,x\}$(zeroth, first and second moments, here along x)
$p1D(x) = mat^{-1} \cdot v1D(x)$(projected densities onto coordinate axes, here x)

Example from Fig. 4b: $p1D(1.07292) = \{0, 0.92708, 0.07292\} \equiv \{px_1, px_2, px_3\}$
$p1D(0.808117) = \{0.191883, 0.808117, 0\} \equiv \{py_1, py_2, py_3\}$

back projected plaquette densities:
$bp(x,y) = \{px_1py_1, px_2py_1, px_3py_1, px_1py_2, px_2py_2, px_3py_2, px_1py_3, px_2py_3, px_3py_3\} =$
$Outer(p1D(y), p1D(x))$
(numerical values in this example are identical to the results from LP shown in Eq. 2b)

<u>*Full result in 2D*</u>: $fmV_{2D}(x,y) = \{mV_{2D}(x,y), bp(x,y)\}$

Table 3 lists the steps used to get Eulerian grid densities beginning with $mV_{1D}(x)$, followed by computation of spatial moments 0, 1, 2 along the coordinate axes, $v1D(x)$ and $v1D(y)$, forward projections of density onto the coordinate axes $p1D(x) \equiv \{px_1, px_2, px_3\}$

and $p1D(y) \equiv \{py_1, py_2, py_3\}$, and finally the back projected densities obtained using an outer product of forward projections. The full result, $fmV_{2D}(x,y)$ in two dimensions, outputs both the minVAR values and back projected cell densities, $bp(x,y)$, following the convention of Eq. 2a. $\mathrm{LP}_{2D}(x,y)$ and $fmV_{2D}(x,y)$ give identical results, with the latter showing a 1000-fold gain in computational speed.

Two properties of the minVAR function (mV for short) are worth noting here: (1) the expression for $mV_{1D}(x)$ is easily recovered from $mV_{2D}(x,y)$ upon noticing that the squared vertical distance from a corner to the midpoint of one of its vertical edges is $\Delta_y^2 = 0.25$. Substituting this value into the expression for $mV_{2D}(x,y)$ gives $mV_{1D}(x)$ by the Pythagorean theorem. A similar argument applies to the recovery of $mV_{1D}(y)$. By extension, $mV_{1D}(x)$ is recovered from $mV_{3D}(x,y,z)$ using $\Delta_y^2 = \Delta_z^2 = 0.25$. (2) $mV_{3D}(x,y,z) = mV_{3D}(x+n, y+m, z+l)$, and similarly for lower dimensions, where *n, m,* and *l* are any positive or negative integers. This identity, especially useful when working with large grids, is based on the translational symmetry previously described, and captured here by the $Floor$ function defined in the table. Finally, it's clear by inspection that $mV_{3D}(x,y,z) = mV_{1D}(x) + mV_{1D}(y) + mV_{1D}(z) = mV_{2D}(x,y) + mV_{1D}(z)$, etc. Solutions need only be computed in 1D and back projected for results in higher dimension. The analytic process here is equivalent to time/operator splitting in QUS. On the other hand, minVAR doesn't require time splitting to work in higher dimension. It is applied directly to random points at sub-grid scale in Sec. 4.1, and can equally well be applied to a non-uniform sequence of points along a curved wind trajectory as suggested in Fig. 4. In this last sense, minVAR can be thought of as providing a unique one-to-one mapping from Lagrangian trajectories to Eulerian grid densities. Quantities not easily captured by the trajectories, e.g. sub-grid turbulence and entrainment, may be better captured by mapping to the grid – and vice versa.

When referring to minVAR in the following sections, unless specified, we are referring to either method LP or mV. LP is more general and will likely have advantages as a development tool in future applications of the method, as it did here. Numeric and analytic

calculations presented in the following section rely mostly on the closed-form mV and fmV algorithms of Table 3 both for their ease of implementation and great computational speed.

4. Applications

The previous section described minVAR's Eulerian representations of point singularities located on one, two, and three dimensional grids. These representations, being purely mathematical in nature, are devoid of physical content. That will change with consideration of multi-point physical representations of aerosols and clouds developed at arbitrarily fine sub-grid scales in Sec. 4.1. Dual LP, equivalently dual minVAR, is introduced to obtain the sensitivity of minVAR values to particle motions across the grid in Sec. 4.2. Finally, the problem of advecting a mixture of distinct aerosol types, each having its own identifiable sequence of interrelated moments is described in Sec. 4.3. Similarities and differences between the minVAR, basic, and QUS schemes in this regard are also discussed.

4.1 Separation and tracking of variance from physical processes using minVAR: This subsection illustrates how sub-grid information can be represented in minVAR parameterically, or on a particle-by-particle basis, the latter using spatially-distributed, multi-point configurations that can represent individual aerosol particles and cloud droplets or sparse representations of their distributions using adaptive quadrature. Such extended systems carry their own physical variance and covariance in addition to their pointwise innate variance contained in minVAR itself. The linearity feature of minVAR allows these different contributions to be tracked separately through multiple grid boxes of volume $\Delta V = \Delta X \Delta Y \Delta Z$ using the methods developed here and in Sec. 4.2.

Figure 6 shows a collection of 1000 particles (black dots) sampled from a binormal distribution having mean, $\{\mu_1, \mu_2\} = \{1.2, 0.88\}$, and covariance matrix elements from Eq. 3

$$\begin{pmatrix} \sigma_1^2 & \rho\sigma_1\sigma_2 \\ \rho\sigma_1\sigma_2 & \sigma_2^2 \end{pmatrix} = \begin{pmatrix} 0.0625 & 0.05625 \\ 0.05625 & 0.0625 \end{pmatrix} \qquad (3a)$$

where ρ is any number between -1 and 1, here ρ =0.9. The parameters on the left of Eq. 3a, generally time dependent, may be tracked directly, without sampling the distribution, using adaptive sigma-point quadrature [Yoon and McGraw, 2004a, b]. The limitation of parameterization, though extremely efficient, is that the distribution shape may morph from binormal to a very different form, necessitating reparameterizations over time. The use of many more points affords much greater accuracy and flexibility in this regard, as does quadrature. Both approaches are remarkably fast, when minVAR is used. Quadrature, with significantly fewer points, is of course much faster. Both particle-by-particle aerosol/cloud tracking and adaptive sigma-point quadrature employ the same sets of lower-order mixed moments, and these evolve over time with closure independent of any parameterized form.

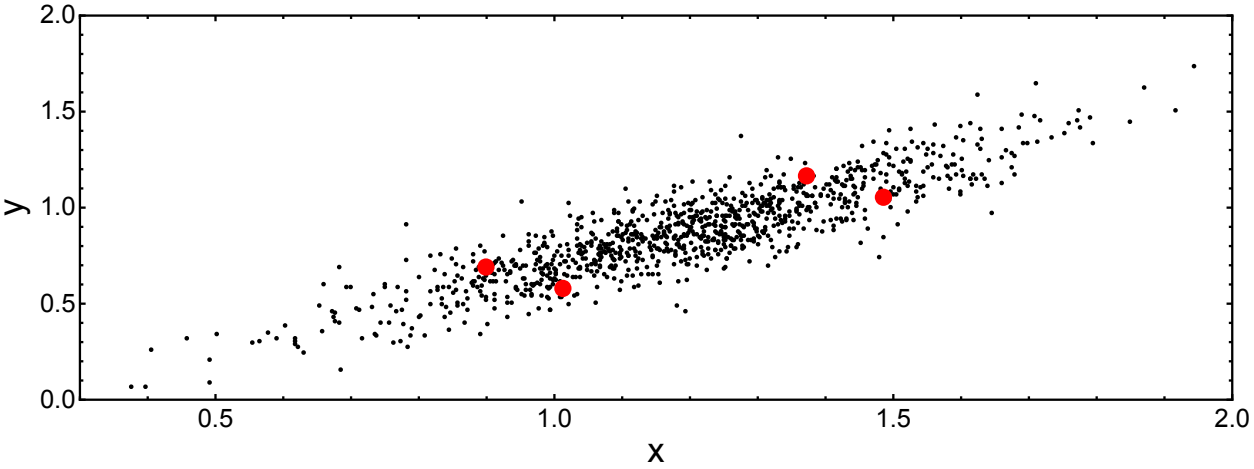

Fig. 6. Sampled set of 1000 points from the parameterized binormal distribution of Eq. 3a (black dots) and four adaptive quadrature points (red dots) having the same six lower-order moments $\{normalization, \langle x\rangle, \langle y\rangle, \langle xx\rangle, \langle yy\rangle, \langle xy\rangle\}$. The quadrature points have equal weights, ¼ each, and lie at corners of a rectangle, distorted here by the different x- and y- axes scales used in the figure.

The 1000-point sample from the binormal distribution of Eq. 3a has slightly different mean and covariance values due to the random nature of the sampling: $\{\mu_1, \mu_2\} = \{1.19263, 0.872259\}$ and covariance matrix:

$$\begin{pmatrix} \sigma_1^2 & \rho\sigma_1\sigma_2 \\ \rho\sigma_1\sigma_2 & \sigma_2^2 \end{pmatrix} = \begin{pmatrix} 0.0592442 & 0.0530498 \\ 0.0530498 & 0.0598873 \end{pmatrix} \qquad (3b)$$

The 1000 particle sample (black points), and its 4-point quadrature representation (red points), shown in Fig. 6, have the same six lower-order moments (normalization, mean values, and covariance matrix elements). The sparse quadrature representation is generated in the principal frame and transformed back to the original frame of the sampled distribution using sigma-point quadrature. Here the form of the distribution doesn't matter, only its moments matter. As the 1000 particles evolve spatially over time, so do the quadrature points, which continue to follow the same lower-order moments, independent of how location and shape of the distribution change over time [Yoon and McGraw, 2004a, b]. Figure 6 represents a snapshot of what the distribution and its sparse representation might look like at a snapshot in time.

For a single point the difference between minVAR values calculated directly from $mV_{2D}(x,y)$ and from the plaquette densities on the Eulerian grid vanishes. This can be checked using the numbers in Eq. 2b, which apply to a single point. Substitution gives:

$$\sum_{i=1}^{9}(x_i^2 + y_i^2)p[i] \; - \; (\mu_x^2(t) + \mu_y^2(t)) \; - \; mV_{2D}(x,y) \; = 0, \qquad (4)$$

which is consistent with the physical variance of the point being zero. The averaged minVAR over 2 or more points no longer equates to the correspondingly averaged back projected densities. The latter is always larger.

To demonstrate, it is instructive to look at $fmV_{2D}(x,y) = \{mV_{2D}(x,y)\,, bp(x,y\}$ averaged over the thousand point sample of Fig. 6,

$$\langle fmV_{2D}(x,y)\rangle = (\sum_{i=1}^{1000} fmV_{2D}(x_i,y_i))/1000. \qquad (5)$$

The centroid of the 1000-particle sample, corresponding to the black points of Fig. 6, has coordinates $\{\mu_1, \mu_2\} = \{1.19263, 0.872259\}$ and a *physical* variance $(\sigma_1^2 + \sigma_2^2) = 0.0119131$ given by the sum of the diagonal elements of Eq. 3b. The aim here is to demonstrate recovery of this physical variance using minVAR. The 1000-point averaging yields averages over the point-by-point minVAR values, $\langle mV_{2D}(x,y)\rangle$, and over the back projected densities $\langle bp(x,y)\rangle$. For the former, averaging over the black points gives:

$$\langle mV_{2D}(x,y)\rangle = (\sum_{i=1}^{1000} mV_{2D}(x_i,y_i))/1000 = \langle minVAR\rangle \; = 0.30007 \qquad (6a)$$

For the latter, averaging over the plaquette densities point-by-point gives:

$$\langle bp(x,y)\rangle = \{0.016, 0.145, 0.0126, 0.0141, 0.581, 0.185, 0, 0.021, 0.025\} \qquad (6b)$$

Using these averaged p[i] values from 6b and subtracting the point-averaged minVAR from 6a gives:

$$\langle \sum_{i=1}^{9}(x_i^2 + y_i^2)p[i] \; - \; (\mu_x^2(t) + \mu_y^2(t))\rangle - \langle mV_{2D}(x,y)\rangle = 0.0119131. \qquad (6c)$$

Unlike with the single-point case of Eq. 4, this difference is always positive. Here it's values precisely equal to the physical variance associated with the spatial distribution of points, which was obtained previously from the sampled distribution by summing the diagonal elements of the variance-covariance matrix of Eq. 3b.

Regarding the covariance, note that taking the inner product of the 9-element array, $\{xy\} = \{0, 0, 0, 0, 1, 2, 0, 2, 4\}$ and $\langle bp(x,y)\rangle$, and subtracting from this the product of the *x*- and *y*- mean values of the 1000-point distribution, gives exactly the covariance of the averaged plaquette densities, 0.0530498 as previously obtained from the sampled distribution by noting its equivalence to the off-diagonal elements of Eq. 3b. In this case no subtraction of the averaged minVAR covariance, which vanishes due to the zero covariance condition invoked in Table 2, is required.

Collectively, these features enable the separation and tracking of the physical variance and covariance arising from aerosol and cloud processes that may include dissipation from wind shear and/or physical diffusion associated with turbulent mixing and entrainment, independent of minVAR's innate variance, a mathematical quantity essential to development of the new advection scheme but devoid of physical content. Additionally, each point from the distribution maintains its individual properties recorded in and recoverable from the coarse grid. Summing these together they represent the distribution itself – a nice illustration of the superposition principle that holds for non-dispersive linear models. The 4-point quadrature approximation not only speeds up the calculation, by an additional 30x as compared with the 1000-point calculation, it produces the same numerical values as

averaging over the 1000-point distribution itself, shown in Eqs. 6, due to the fact that the four adaptive quadrature points are tracking the same spatial moments.

4.2 Dual LP and dual minVAR: Each LP comes with its unique dual program, constructed from it using the same I/O, see for example [Bazaraa, et. al., 2010] for rules of construction. For present purposes, the most important result from the dual LP is sensitivity of the minVAR cost function to changes in location as individual point particles follow wind trajectories across the grid. Figure 7 shows the minVAR contours from Fig. 5 superposed with the dual minVAR solution described below.

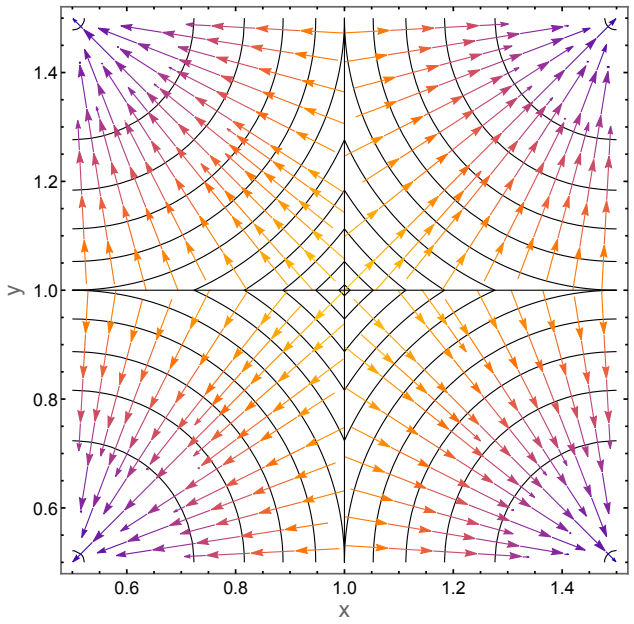

Fig. 7. Primal-dual solutions to minVAR. Comparing the primal solution for minVAR (black contours as in Fig. 5) with the dual solution for sensitivities (gradient vector field) superposed. Colors represent the vector norm, which is smallest, equal to zero, at the corners (purple) and largest, equal to $\sqrt{2}$ at the center (yellow). Horizontal and vertical lines highlight the four quadrants and symmetries of the minVAR solutions.

Analytic solution for the dual: The simplicity of the analytic forms for minVAR, evident in Table 3, make it unnecessary to go through the dual LP, as the desired sensitivities are easily

obtained directly from the analytic result. Denoting these sensitivities as $v_x = \frac{\partial\, mV_{2D}(x,y)}{\partial\, x}$ and $v_y = \frac{\partial\, mV_{2D}(x,y)}{\partial\, y}$, and taking derivatives of the expressions in Table 3 gives:

$$v_x = 2(1/2 - x + Floor[x]) = 2(a_x - x)$$
$$v_y = 2(1/2 - y + Floor[y]) = 2(a_y - y) \qquad (7)$$

for components of the contour gradient vector in 2D. $Floor[x]$ changes discontinuously at integer values of *x*, a feature responsible for the piecewise parabolic structure of minVAR, seen in the red dashed curve of Fig. 3b, and discontinuous changes in v_x and similarly, in 2D, for v_y. The minVAR curves are in fact obtainable by integration over the gradient vector field described by Eq. 7. Sensitivity vectors having components given by Eq. 7 are plotted using the StreamPlot feature of *Mathematica* in Fig. 7 and superposed on the minVAR contours. One sees that the gradient field and minVAR circles are mutually orthogonal to each other. They are in fact each other's dual, reflective of the textbook property that the dual of the dual program gives the "primal" or original program back again [Bazaraa, et al., 2010]. From Eq. 7 and definition of the sensitivities given above:

$$d\, mV_{2D}(x,y) = v_x dx + v_y dy\,, \qquad (8)$$

which vanishes along the circular contours of constant minVAR. For if *r* is the radial distance from the nearest corner $\{a_x, a_y\}$, the directional derivative along line $r(\theta)$ has the form:

$$\frac{d\, mV_{2D}(x,y)}{dr} = v_x \sin\theta + v_y \cos\theta \qquad (9)$$

where θ is the angle the line makes with the vertical axis. Equations 8 and 9 are equivalent to the result that $d\, mV_{2D}(x,y)$ vanishes along any circular contour, *dr = 0*. This demonstrates that properties of the primal (circular contours of constant minVAR centered on the staggered network of cell corners) can be deduced from the conjugate properties of the dual (sensitivities) and vice versa.

Restoring dimensionality to the grid coordinates, x and y, gives the true distances (meters) from the grid origin to $\{x\Delta X, y\Delta Y\}$ where ΔX and ΔY are the actual grid spacings. The time derivative of minVAR is then:

$$d\ mV_{2D}(x,y) = \frac{\partial\ mV_{2D}(x,y)}{\partial\ x}\ u\ dt\ +\ \frac{\partial\ mV_{2D}(x,y)}{\partial\ y}\ v\ dt, \qquad (10)$$

where $u = \Delta X dx/dt$ and $v = \Delta Y dy/dt$ are the corresponding wind velocity components taken at each sampled point along a wind trajectory and inputted to the advection algorithm at time intervals *dt*.

Figure 7 shows primal-dual results for the center grid cell. The gradient vector field for neighboring cells follows the same translational symmetry as the grid itself. The gradient vectors point from the least diffuse state at cell center (minVAR = 0) to the most diffused states located at the cell corners (minVAR = ½ in 2D). Though of purely mathematical origin, the direction these vectors take is the same as would any physical variance increasing with time according to the second law (increased variance corresponding to increased entropy in the physical case). Time-dependent increases in physical variance due to irreversible microphysical and fluid-dynamical processes, such as diffusive mixing from entrainment and energy dissipation from shear, are separable from the minVAR gradients shown in the figure, in much the same way that mathematical and physical contributions to the variance itself were separated in Sec. 4.1. Development of the most efficient ways to represent dissipative processes in sub-grid models based on this separation will be considered in future studies.

4.3 Preserving moment sequence correlations during advection: The testing of tracer advection schemes typically involves the transport of individual tracers in one or two dimensions, often with periodic boundary conditions [Rood, 1987] - a reasonable approach given that the schemes undergoing such testing were never designed to preserve correlations between a sequence of tracers from an interrelated set. The QUS scheme, discussed in Sec. 2 has been subject to tests of this type including simple clock rotation and pure advection in 2D [Shia et al., 1990]. Testing for preservation of correlations between sets

of interrelated tracers during advection, has been limited largely to those few papers mentioned in Sec. 1. Here we apply a test devised by Wright (2007), originally to assess the integrity of correlated moments under vector transport involving one or two lead moments. McGraw (2007) used non-negative least squares (NNLS) [Lawson and Hanson, 1995] to assess the effect of transporting four moments from identifiable sequences associated with each of three distinct aerosol types employed in the test. Not surprisingly NNLS performed better than vector transport using just one or two lead moments, but all of these tests showed levels of moment set reconstruction far from perfect [Wright, 2007; McGraw, 2007, 2012]. The goal of the Wright and McGraw studies was to identify and correct corrupted moment sequences. The aim in this section is to showcase minVAR as an entirely new transport algorithm, designed explicitly to preserve tracer correlation, and thereby obviate any need for moment correction.

Wright's correlation test considered an external mixture of three aerosol types each characterized by a unique lognormal distribution and corresponding sequence of four radial moments $\{\mu_0, \mu_1, \mu_2, \mu_3\}$ where $\mu_k = \int_0^\infty r^k f(r) dr$. In vector form these sequences are:

$$\begin{aligned} \mathrm{v}_1 \text{ (red)} &= \{1.0\text{x}10^6, 30802.2, 9001.71, 24959.3\}^{\mathrm{T}} \\ \mathrm{v}_2 \text{ (green)} &= \{1.0\text{x}10^4, 10106.2, 260788.0, 1.71832\text{x}10^8\}^{\mathrm{T}} \\ \mathrm{v}_3 \text{ (blue)} &= \{1.0\text{x}10^3, 151.593, 586.774, 57993.2\}^{\mathrm{T}}. \end{aligned} \tag{11}$$

where the superscript T stands for transpose. Colors refer to the histogram plots of Figs. 9 and 10. As this a pure advection test case (without microphysical processes) the moments for each aerosol type, though they mix, remain proportional throughout the simulation. For the initial condition (M_0), 20 grid cells are populated with just one aerosol type in each cell. The types are distributed according to the following 4x20 matrix:

$$\mathrm{M}_0 = \{\, \mathrm{v}_3, \mathrm{v}_3, \mathrm{v}_1, \mathrm{v}_2, \mathrm{v}_3, \mathrm{v}_3, \mathrm{v}_3, \mathrm{v}_3, \mathrm{v}_3, \mathrm{v}_3, \mathrm{v}_3, \mathrm{v}_3, \mathrm{v}_3, \mathrm{v}_3, \mathrm{v}_3, \mathrm{v}_3, \mathrm{v}_3, \mathrm{v}_3, \mathrm{v}_3 \}. \tag{12}$$

Advection is carried out using periodic boundary conditions and the wind direction and Courant number are as in Fig. 1. Thus with each advection step 15% of the tracers of cell 20 get transferred to cell 1 and 85% stays in cell 20. Throughout the calculation each moment

562 is transported as an independent tracer before going on to the next moment and the results
563 are combined to update M after each step.
564
565 Wright's test is now employed to test advection of moments both as independent
566 tracers and for loss of correlation. The four panels of Fig. 8 show the advection test applied
567 to each of the four radial moments $\mu_0, \mu_1, \mu_2, \mu_3$ advected separately across the grid as
568 independent tracers. The two histograms in each panel are results for advection using QUS,
569 solid black, and minVAR, dashed red. As with the pulse test comparison of Fig. 3a, both
570 models show numerical diffusion well under control. The absence of any broadening near
571 baseline reflects the complete absence of numerical diffusion using minVAR.

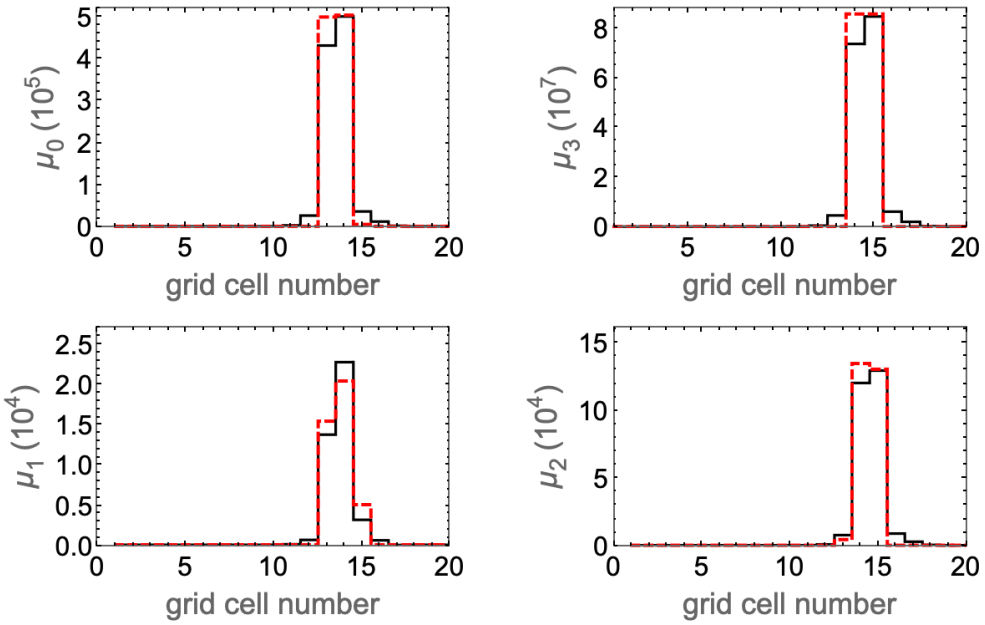

Fig. 8. Individual transport of each of the four radial moment tracers under QUS (solid black) and minVAR (dashed red) histograms each representing the full externally mixed aerosol population. Results are shown after completion of 70 advection steps. Upper row: particle number, μ_0, and μ_3, proportional to particle volume. Lower row: μ_1, radial moment, and μ_2, proportional to particle surface area.

572 The quantification of dispersion is more difficult to assess for the tracer mixture than
573 it was for the single-tracer pulse test comparison of Fig. 3b. The histogram shapes in Fig. 8
574 tend to differ for each moment. An exception is seen in moments μ_0 and μ_3 , which have
575 similar shapes irrespective of whether they were advected by QUS or minVAR. These

moments turn out to be spatially shifted from each other by almost exactly one grid spacing — equivalent to the one full cycle shift in phase expected from Fig. 3b. This suggests strong linkages between dispersion, phase shift, and distribution shape. Fig. 3b also shows a nearly constant shift in phase between the two advection schemes that could well be responsible for the different histogram shapes within each of the moment panels of Fig. 8.

Correlation loss is examined next. This test requires projecting each of the three aerosol types from the advected columns of M_{70}, the updated version of M_0 after 70 advection steps. Let $\mathbf{A} = [\mathbf{v}_1, \mathbf{v}_2, \mathbf{v}_3]$ be the 4 by 3 matrix consisting of the length 4 moment arrays for each of the 3 pure aerosol type as columns, and $\mathbf{b}_j$ the j^{th} column vector of the moments in cell j after any given number of advection steps (here 70). NNLS can be used to do a forensic analysis to project out the different types of aerosol present in each of the columns of M_{70}. Errors due to loss of moment correlation will also be uncovered during this process when higher-order advection schemes are employed. The method, originally used as a way to correct corrupted moment sequences, was applied to QUS previously [McGraw, 2007]. Figures similar to those shown in the first row and lower left quadrant of Fig. 9 were also given in that paper. NNLS solves the following linear system:

$$\mathbf{A}\,\mathbf{c} = \mathbf{b}_j + \mathbf{e}, \tag{13}$$

obtaining the coefficient vector $\mathbf{c} = (c_1, c_2, c_3)^T$ that minimizes the Euclidean norm of the error residual, $\mathbf{e}$. Use of NNLS insures non-negative coefficients c_i .

Ideally, as the aerosols and their moment sequences mix but are not changed in the test, error residuals should vanish to give the fraction of each aerosol type present in each cell. This is the case for the two linear models, basic and minVAR, and the aerosol composition in each cell is completely resolved into the original aerosol types ($\mathbf{e} = 0$):

$$\mathbf{b}_j = \mathbf{A}\,\mathbf{c} = c_1\,\mathbf{v}_1 + c_2\,\mathbf{v}_2 + c_3\,\mathbf{v}_3. \tag{14}$$

In this case a simpler least-squares error procedure, based on the pseudoinverse of $\mathbf{A}$, suffices to do the decomposition [Strang, 1988]. With the higher-order advection schemes,

606 including QUS, negative coefficients occur often and NNLS must be used to insure non-
607 negative coefficients.

608 For the present analysis NNLS and pseudoinverse gave identical results for the
609 minVAR scheme. For QUS the pseudoinverse was inapplicable and NNLS was required. The
610 R, G, and B histograms of Fig. 9 plot the coefficients, c_1, c_2, and c_3, respectively, for each
611 column of M_{70}, as obtained from advection using QUS.

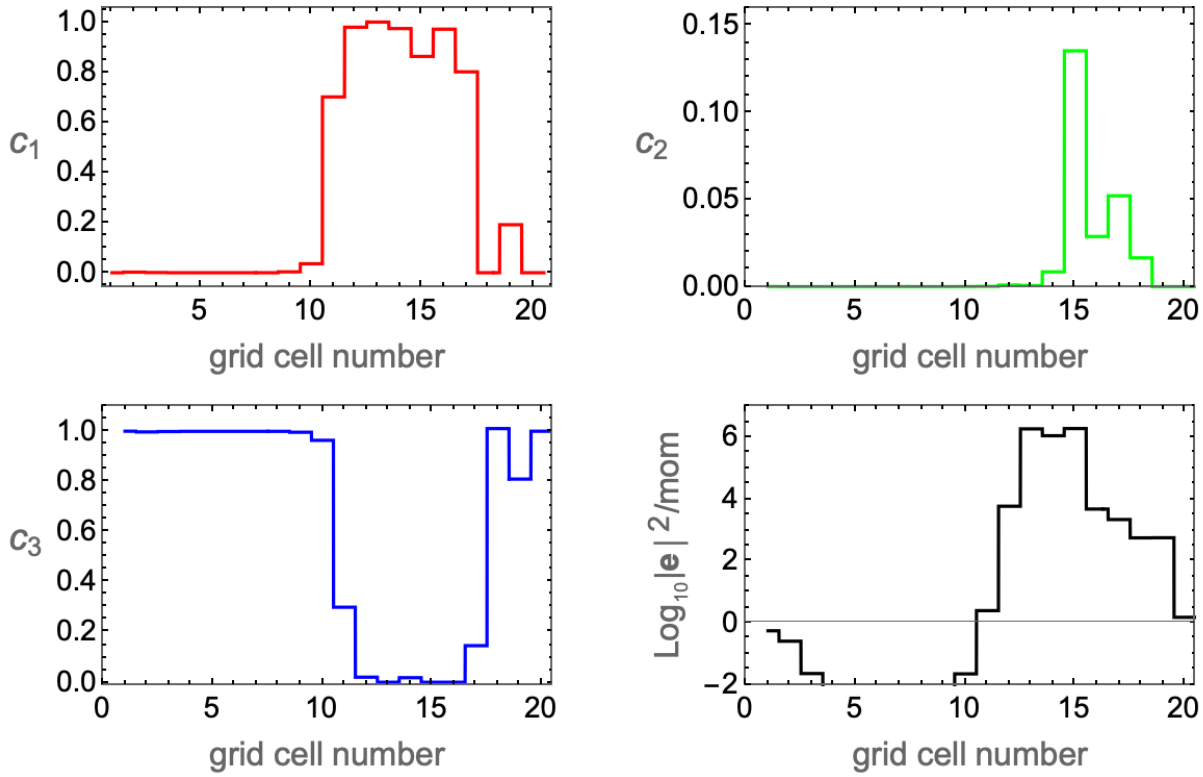

Fig. 9. Results from QUS after 70 advection steps. The coefficient distributions, c_1 – c_3 refer to use of normalized moments. These were projected from the mixture in each grid cell using NNLS decomposition following McGraw (2007). The lower right quadrant shows distribution of mean squared error, divided by 4 to average over the 4 moments per column, following advection of the original (unnormalized) distributions. The wrap-around effect from the period boundary conditions is evident in the panels.

612

613 The lower right quadrant of the figure shows the mean squared error residuals from Eq. 13
614 plotted on a logarithmic scale. These coefficients are seen to be dispersed over an
615 unphysically wide swath of the grid. This and the significant level of mean-squared error are
616 indicative of significant loss of moment sequence preservation.

A test for unphysical moment sequences was also carried out for each of the 20 columns of M_{70} and none were found. It should be noted, though, that finding unphysical moments in even a single column of the 20 would be a 5% failure rate, whereas Wright reported failure rates closer to 1% for QUS, based on his analysis of an ensemble of 10^4 test cases [Wright, 2007]. The moment sequence viability test is as follows: A necessary and sufficient condition for physicality of a moment sequence is that certain Hankel-Hadamard determinants constructed from the moments be positive [Shohat and Tamarkin, 1943; McGraw, 2012]. For physicality of the sequence $\{\mu_0, \mu_1, \mu_2, \mu_3\}$, the requirement is that each of the four elements of the following determinant sequence be positive:

$$\left\{\mu_0, \begin{vmatrix} \mu_0 & \mu_1 \\ \mu_1 & \mu_2 \end{vmatrix}, \mu_1, \begin{vmatrix} \mu_1 & \mu_2 \\ \mu_2 & \mu_3 \end{vmatrix}\right\} \geq 0\,. \qquad (15)$$

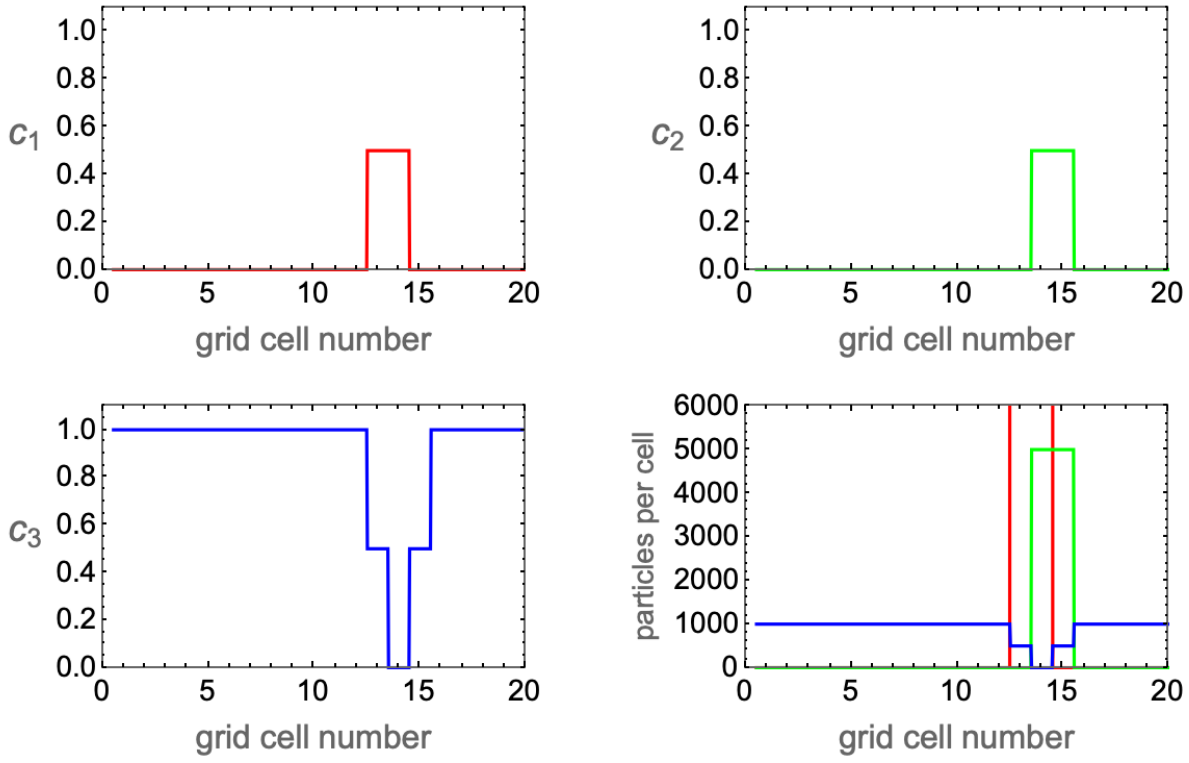

Fig. 10. Results from minVAR after 70 advection steps. The coefficient distributions, c_1 – c_3 refer to use of normalized moments as in Fig. 9. These were projected from the mixture in each grid cell using NNLS decomposition following McGraw (2007), but in this case the pseudoinverse is simpler to use and gave equivalent results. The lower right panel shows the unnormalized distributions.

628 Figure 10 shows results from a similar calculation, with M_{70} computed from the same
629 initial condition, M_0, but updated at each time step according to the new minVAR scheme.
630 The R, G, and B histograms of Fig. 10 again show the coefficients, c_1, $c_{2,}$, and c_3 plotted for
631 each grid cell. In this case there is minimal coefficient dispersal over the grid and zero mean
632 square error ($\mathbf{e} = 0$) indicative of full moment sequence preservation. Consistent with linear
633 superposition, the red and green fractions each sum to unity as each occupied single grid
634 cells (3 and 4 respectively) at t=0. The blue fractions sum to 18 as blue occupied the 18
635 remaining cells initially. The lower right quadrant shows results for the original
636 (unnormalized) distributions. Red is off scale at 5.0×10^5. Extension to 80 or any multiple of
637 20 advection steps would show a shifted but perfectly reconstructed version of the initial
638 condition. Advection was carried out using the same periodic boundary conditions as in Figs.
639 8 and 9 and under the same wind direction and Courant condition as in Figs. 1-3.
640
641 **5. Summary and discussion**
642 Key features of the minVAR limiter discussed in this paper may be summarized as
643 follows: (1) As applied to the linear basic advection scheme, minVAR was found to eliminate
644 numerical diffusion completely while preserving the best features of that scheme including
645 linearity and lack of dispersion (Sec. 2). The latter feature, achieved by not having to
646 reference higher-order gradients, which will typically differ for different tracers of an
647 interrelated set, is key to the preservation of tracer correlation (Sec. 4). (2) The minimum
648 variance property of minVAR makes the new method optimal for advection of independent
649 tracers as well as correlated ones (cf. Figs. 3 and 8 for a comparison with QUS in this regard).
650 As minimal spatial variance implies maximal spatial resolution, this feature suggests
651 minVAR, which preserves resolution at just 1-2 grid spacings throughout the coarse a
652 simulation, could well replace the more slowly convergent basic scheme for modeling at the
653 fine scales of laboratory and engineering simulation. (3) As a point-by-point method,
654 minVAR establishes a unique one-to-one correspondence between points along a Lagrangian
655 trajectory and their representation on an Eulerian grid. This direct correspondence allows
656 the best features of Lagrangian and Eulerian methods to reinforce each other in simulations.
657 (4) The extension from single points to multi-point representations of aerosol and clouds

enables a rigorous and complete separation of physical variance from the innate mathematical variance associated with minVAR's representation of points on the Eulerian grid. (5) minVAR's maximum of two adjacent occupied cells per dimension were found sufficient to pinpoint the coordinates of the point being represented (Sec. 3) at a level of resolution limited only by numerical precision.

The last property is reminiscent of an early method developed for analyzing the numerical calculation of hydrodynamic shocks in one dimension [von Neumann and Richtmyer, 1950]. Their idea was to add artificial (and nonlinear) dissipative terms to the hydrodynamic equations so as to *broaden* the shock front discontinuity, a point singularity in 1D, to "a thickness comparable to, but preferably somewhat larger than the spacing of the points of the network" used in their model. The effect was to made locating the shock singularity immediately evident as it moved through the fluid.

Most advection schemes in common use introduce nonlinearity at some stage of the process (Sec. 1). Errors during advection of independent tracers for which these schemes were designed are usually tolerable, but once even a small error enters into an interrelated tracer set it grows exponentially to infect other members of the set and information available at the start of the simulation is destroyed. The problem is discussed in Lanczos [Lanczos, 1988] and gets worse the higher the order of the scheme [Wright, 2004]. Exponential error amplification during finite differencing is illustrated for a sequence of six moments from a lognormal distribution in [McGraw, 2012]. Similar considerations are important when selecting a microphysical module to update aerosol and cloud particle properties between advection steps. Modal, moment, particle-resolved, and quadrature-based methods, all of which perform well as box models for updating the contents of a grid cell between steps, should be fully compatible with minVAR. An interesting question for future research concerns the extent to which minVAR can be used to eliminate numerical diffusion in bin-sectional models of aerosol and cloud microphysical processes, a well-known problem especially for particles undergoing condensational growth.

In summary, a linear diffusion limiter has been developed and applied to the basic advection scheme. The new result (minVAR) has been shown here to be non-diffusive, non-dispersive, preserving of tracer set correlations, and capable of tracking sub-grid information at arbitrarily fine scales with high computational efficiency. We expect these new capabilities, fully implemented, to considerably advance progress towards achieving high-fidelity representations of aerosols and clouds in atmospheric transport models.

Open Research Statement

Computer codes for minVAR implementation and figure generation are available at https://doi.org/10.5281/zenodo.7607752

Acknowledgements:

R. McGraw (BNL) and F. Yang (BNL) acknowledge the Atmospheric Systems Research (ASR) Program of the U.S. Department of Energy (Grant No: DE-SC0012704) for financial support. L. M. Fierce (PNNL) is supported by the U.S. Department of Energy Office of Science Biological and Environmental Research as part of the Atmospheric Systems Research (ASR) Program. Pacific Northwest National Laboratory is operated by Battelle for the U.S. Department of Energy under Contract DE-AC05-76RLO1830.

References:

Bazaraa, M. S., Jarvis and Sherali, H. D. (2010), *Linear Programming and Network Flows* (Wiley, Hoboken) Chapter 6.

Bott, A. (1989a), A positive definite advection scheme obtained by nonlinear renormalization of the advective fluxes. *Monthly Weather Review, 117*, 1006-1015.

Bott, A. (1989b), Reply. *Monthly Weather Review, 117*, 2633-2636.

Chandrasekhar, S. (1943), Stochastic problems in physics and astronomy. *Rev. Mod. Phys. 15* (1), pp 79-80: Appendix I, The mean and mean square deviation of a Bernoulli distribution.

Lanczos, C. (1988), *Applied Analysis*, Chap. 5, pg. 313 (Dover, New York, 1988).

Lawson, C. L. and R. J. Hanson (1995), Solving Least Squares Problems (SIAM, Prentice-Hall, Englewood-Cliffs, New Jersey) Chapter 23.

McGraw, R. (2007). Numerical advection of correlated tracers: preserving particle size/ composition moment sequences during transport of aerosol mixtures. In *Journal of physics: Conference series* (Vol. 78, p. 012045). doi: 10.1088/1742 -6596/78/1/012045

McGraw, R. (2012). Correcting transport errors during advection of aerosol and cloud particle moment sequences in Eulerian models, In *Climate Models*, edited by L. M. Druyan, Chapter 13, pp. 297-310.

Ovtchinnikov, M. and Easter, R. C. (2009). Nonlinear advection algorithms applied to interrelated tracers: Errors and implications for modeling aerosol– cloud interactions. *Monthly weather review, 137*(2), 632–644. doi: 10.1175/2008MWR2626.1

Prather, M. J. (1986). Numerical advection by conservation of second-order moments*. J. Geophysical Research, 91*, 6671-6681.

Rood, R. B. (1987). Numerical advection algorithms and their role in atmospheric transport and chemistry models. *Reviews of Geophysics, 25*, 71-100.

Russell, G. L. and Lerner, J. A. (1981). A new finite-differencing scheme for the tracer transport equation. *J. Applied Meteorology 20*, 1483-1498.

Shia, R-L., Ha, Y. L., Wen, J-S. and Y. L. Yung (1990. Two-dimensional atmospheric transport and chemistry module: Numerical experiments with a new advection algorithm. *J. Geophys. Res. 95*, 7467-7483.

Shohat, J. D. and Tamarkin, J. D. (1943). *The problem of moments* (American Mathematical Soc., New York) pg. viii.

Strang, G. (1988). *Linear algebra and its applications (3rd edition)*. (Thomson Learning, Inc., USA) Appendix A.

von Neumann, J. and Richtmyer, R. D. (1950), A method for numerical calculation of hydrodynamic shocks. *J. Applied Phys. 21*, 232-237.

Wright, D. L. (2007). Numerical advection of moments of the particle size distribution in Eulerian models. *J. Aerosol Science 38*, 352-369.

Yang, F., Ovchinnikov, M., Thomas, S., Khain, A., McGraw, R., Shaw, R. A. and Vogelmann, A. M. (2022). Large-eddy simulations of a convection cloud chamber: Sensitivity to bin microphysics and advection. *J. Advances in Modeling Earth Systems 14,* e2021MS002895. https://doi.org/10.1029/2021MS002895.

Yoon, C. and McGraw, R. (2004a, b). Representation of generally mixed multivariate aerosols by the quadrature method of moments: I. Statistical foundation, *J. Aerosol Sci. 35*, 561-576; II. Aerosol Dynamics, *J. Aerosol Sci. 35*, 577-598.